High spatial resolution Raman mapping of complex mineral assemblages: application on phosphate mineral sequences in pegmatites

Fernando Prado Araujo[1*], Niels Hulsbosch[1], and Philippe Muchez[1]

[1]KU Leuven, Department of Earth and Environmental Sciences, Division of Geology, Celestijnenlaan 200E - Box 2410, 3001, Leuven, Belgium (*corresponding author: fernando.pradoaraujo@kuleuven.be)

ABSTRACT

Phosphates are a group of complex minerals widespread on Earth that can crystallize in several environments. Changes in environmental conditions during crystallization are reflected in the formation of a sequence of phosphate minerals, termed paragenesis. Accordingly, analyses of textural and chemical properties of complex mineral assemblages are essential to reconstruct the history of rocks and solid materials. Raman mapping can detect those mineralogical changes in complex assemblages with high spatial resolution, successfully determining the paragenetic sequence. Specifically, Raman spectroscopy is more advantageous than conventional methods because it requires little sample preparation, it is non-destructive, and it is capable of identifying hydrated minerals and phases composed of light elements (*e.g.* H, Li). In this study, the parageneses of two phosphatic assemblages from the Buranga pegmatite, a P-Li-Nb-Ta-rich magmatic rock, are reported in detail. The first case shows the replacement of primary F-rich montebrasite [$LiAl(PO_4)(OH,F)$] by secondary F-poor montebrasite [$LiAl(PO_4)OH$]. Mapping of the OH-stretching peak position and width identifies the mineral phases, illustrates their spatial relations, and allows to estimate the F content distribution. The second case investigates a sequence of phosphate minerals in a complex assemblage (trolleite + rosemaryite → lazulite-scorzalite → samuelsonite → wardite). The application of multivariate analysis methods to characterize complex assemblages is assessed, and the classical least squares method is identified as the best suited for this setting. Analysis of Raman images shows that Buranga samples experienced a progressive hydration process during cooling, followed by fluid-assisted mineral reactions with remobilization of elements, such as Ca and Na.

Keywords: Phosphate, mineral paragenesis, Raman mapping, pegmatites, Buranga

1. INTRODUCTION

Phosphates are a diverse mineral group comprising more than 1800 species[1]. Due to their compositional and crystallographical complexity, they have been the focus of many mineralogical and chemical studies[2–5]. Phosphate minerals form an integral component of numerous geological and biological systems. More specifically for geological systems, phosphates occur practically in all rock types and are particularly abundant in sedimentary (*i.e.* phosphorite) and magmatic rocks. In the latter, especially pegmatites are known for their vast and exceptionally rich phosphate mineralogy[6].

As a mineral resource, both phosphorus and phosphate rocks are classified as critical raw materials by the European Commission[7]. Apart from food, chemical and pharmaceutical major end uses, phosphate mineral resources are very important for agricultural purposes as they are the main component of mineral fertilizers[8,9]. Moreover, some phosphate minerals like montebrasite-amblygonite [$LiAl(PO_4)(OH,F)$] were formerly exploited as lithium ore and are again gaining economic interests as alternative lithium sources due to the high demand of lithium for Li-ion battery technology[10–12]. Consequently, to explore and exploit these mineral resources more sustainably, it is necessary to understand phosphate mineral formation and their stability conditions.

In magmatic rocks, phosphates can crystallize in a wide range of environments, including at high temperatures (>500 °C) from the solidifying magma, at intermediate hydrothermal stages (500-50°C) from a fluid phase exsolved from the solidifying magma, and at low temperatures of shallow (sub)surface conditions during weathering processes (<50°C). Therefore, phosphate minerals are commonly used as indicator minerals in petrological studies as they are proxies for the pressure, temperature, and compositional evolution of the magmatic host rock[13–18].

Despite the group's wide range of occurrence, experimental studies have shown that individual phosphate minerals or distinct assemblages can have narrow pressure-temperature-composition (P-T-X) stability fields[19–22]. Primary phosphates, which crystallize in a magmatic environment, can be subsequently replaced by lower temperature phases during the transition from a melt- to a fluid-dominated environment, or later, by supergene minerals under surface weathering conditions[4,6]. This implies that a sequence of phosphate minerals can record the specific pressure-temperature-composition (P-T-X) trajectory of the magmatic rock[3,4]. The relative-time sequence of minerals, or so-called paragenetic sequence, is recorded in the textural relations between the different phosphate minerals.

The integration of paragenesis with the specific crystallization conditions of each mineral can reflect the chemical evolution of the system and express the formation sequence of the rock. However, this integration requires a mineralogical characterization of phosphates with high spatial resolution, since phosphate mineral assemblages can occur from tens of centimeters to few millimeters in size, and exhibit complex textures like replacement, overgrowth, and recrystallization[23–26]. Moreover, many phosphates can have

complex compositions, defined by OH groups or molecular water, crystallographic vacancies, low mass elements (e.g. Li), or transition metals with variable oxidation states (Fe, Mn, etc.), and most chemical techniques are not able to directly measure these components. Consequently, phosphate mineral characterization by most conventional quantitative (micro)analyses, such as backscattered electron microscopy (SEM), electron microprobe analyzer (EPMA), micro or bulk X-ray fluorescence (XRF), laser ablation mass spectrometry (LA-ICP-MS), or X-ray diffraction (XRD), is challenging as these techniques rely on the chemical characterization of the elemental composition or are bulk techniques. More specifically, elemental chemical methods require the stoichiometric calculation of the mineral formula, which inherently is founded on certain assumptions[27] (*e.g.* site assignment for multi-site cations or the molecular proportions of multi-oxidation state elements) resulting in potential ambiguous identifications of complex phosphate minerals. Crystallographic methods, such as XRD, can characterize complex structures and identify specific phosphate minerals, but lack the high spatial resolution or require extensive sample preparation before analysis. Problems with standardization and matrix effects can also hinder geochemical analysis in almost all the methods described before[28], as phosphate standards are uncommon and can knowingly be damaged from recurrent analyses[29].

Confocal micro-Raman analysis, in turn, provides molecular information at a high spatial resolution without losing the textural context (*i.e. in situ* analysis), easily characterizing complex minerals[30,31] and phosphate assemblages[32–34]. Raman spectroscopy has many applications in geosciences, and its use is increasing throughout the years[35]. The recent analytical developments of hard- and software integrations, such as fully confocal microscopic setups, high-speed and high-precision XYZ scanning stages, charge-coupled device (CCD) detectors with improved electronic gain like electron-multiplying (EM) CCDs, high-resolution gratings, and long focal length spectrometers, allow fast attainment of Raman spectra (~0.1s acquisitions) with high spectral and spatial resolution, opening the possibility to high definition Raman maps in realistic acquisition times and with low user costs. These advancements in confocal micro-Raman spectroscopy enable to fully apply this technique in mineralogical and paragenetic studies of complex mineral groups.

Raman mapping enables precise and accurate measurements of molecular and spatial information of minerals. The hyperspectral images generated provide ways to investigate the molecular changes in the sample, allowing not only the identification of phases but also the visualization of their textural relations.

This study applies state-of-the-art Raman imaging techniques to define the paragenetic sequencing of complex phosphate mineral assemblages in the Buranga pegmatite. The Buranga dike is a Sn-Nb-Ta-bearing pegmatite located in Western Rwanda. It is a key natural case-study for Raman mapping development of complex mineral parageneses as the dike hosts more than 50 individual phosphate species often with complex intergrowth or replacive textures [36]. Moreover, the Buranga pegmatite is a type-locality

for three phosphates (bertossaite: $(Li,Na)_2(Ca,Fe^{2+},Mn^{2+})Al_4(PO_4)_4(OH,F)_4$; burangaite: $NaFe^{2+}Al_5(PO_4)_4(OH)_6 \cdot 2H_2O$ and gatumbaite: $CaAl_2(PO_4)_2(OH)_2 \cdot H_2O$), and many mineralogical and experimental P-T-X stability studies are based on natural Buranga samples[19,37–44].

We present the application and method development of Raman mapping to constrain the mineralogical evolution, *i.e*. the paragenetic sequence, of phosphate minerals. The Raman methodology presented here, moreover, overcomes the analytical issues related to conventional chemical microanalyses to straightforwardly map phosphate assemblages with high spatial resolution. Based on our Raman data, we confirm that these complex mineral assemblages record the evolution of the magmatic host rock and can be used as proxies for pegmatite formation. Additionally, we present a literature overview of the classification of phosphate minerals, discuss their major Raman fingerprint, and compare the effects of different multivariate analyses steps in data treatment on the visualization of complex phosphate assemblages and textures.

2. METHODOLOGY

2.1. Materials and sample location

The research samples are from the Buranga pegmatite, located in the Gitarama-Gatumba pegmatite field of Western Rwanda[45–47]. Phosphate minerals occur as polymineralic nodules at the most internal zone, or so-called core zone, and its transition zones within the Buranga dike, which represents the last stages of magma solidification within a pegmatite dike[48,49]. Samples BU18FA09 and BU18FA19 (sample RG 9705 from the Royal Museum for Central Africa rock and mineral collection) were prepared into rectangular standard-size 27 x 46 mm doubly-polished thick wafers and polished thin sections. To ensure sample transparency for transmitted light microscopy, the final thicknesses are adapted and vary between 30-50 μm for thin sections and 150-200 μm for thick wafers.

2.2. Optical microscopy

Optical analysis was conducted on an Olympus BX40 petrographic polarization microscope with the 5x, 10x, and 50x objectives (Olympus, MPLN) under transmitted white light at the Department of Earth and Environmental Sciences, KU Leuven, Belgium. Physical and optical characterization of minerals included determination of their color, optical relief, cleavage directions, pleochroism, interference color, extinction angle, conoscopic interference pattern, 2V angle, and optical sign.

2.3. Qualitative chemical analysis by energy-dispersive spectroscopy (EDS)

Samples were coated with a ~20 nm layer of carbon, imaged by backscattered electrons (BSE), and analyzed by energy-dispersive spectroscopy (EDS) in a JEOL JXA-8530F field emission gun electron

probe micro-analyzer (EPMA) at the Department of Materials Engineering, KU Leuven, Belgium. X-ray energy was analyzed with a silicon drift type detector, cooled by Peltier effect, under an acceleration voltage of 15 kV and beam current of 5 nA. EDS maps for each element were obtained concomitantly with a total acquisition time of around 17 min (5 ms per pixel). More details on the equipment can be found in Van Daele et al[50]. Standards were not analyzed by EDS, consequently, analyses were only qualitative and no chemical quantification was performed. EDS sample preparation and analyses were performed after the Raman analyses to not affect the Raman signal due to the carbon coating or electron beam damage.

2.4. Raman microscopy

2.4.1. Instrumentation

Raman spectra were obtained using a Horiba Jobin-Yvon LabRAM HR Evolution System, focal length of 800 mm, at KU Leuven. The dispersive Raman spectroscope is installed on an air-compressed kinematic table of the type Kinematic Systems 5100. The spectroscope is coupled to an Olympus BX41 confocal microscope equipped with a Märzhäuser Wetzlar SCANplus motorized XYZ stage. The stage has a travel length and width of 75x50mm and provides, for X and Y, repeatability of <1 µm, an accuracy of 1 µm, and a resolution of 50 nm. The Z resolution is 10 nm.

Samples were excited with an air-cooled, frequency-doubled Nd:YAG laser with a 532 nm wavelength (Oxxius, diode-pumped solid-state laser of 100 mW power) in backscattering geometry. Laser attenuation filters were used to avoid sample overheating and laser damage to the sample, the output laser power was set to either 100% or 25% of the source power. Rayleigh edge rejection filters were used to obtain laser line cut-off lower than 50 cm^{-1}. The scattered signal was measured with a front-illuminated Synapse Electron Multiplying (EM)-CCD detector with 1600x200 pixels (16 µm pixel size) that was Peltier-cooled to -60 °C. The electron-multiplying system provides an extended serial gain of electrons that amplifies the detected light before the readout, increasing the acquired signal. The electron-multiplying (EM) gain value is set by the user between 0 and 1000 and represents the increased probability of new electrons being generated due to the higher potential in the extended serial register. The EM-CCD enables detection between 400-1000 nm and has a quantum efficiency of better than 30% for 500-800 nm and 50% for 700-800 nm. The EM-CCD readout was performed in MPP/AIMO mode to ensure the lowest noise operational capability. The minimum acquisition time of the EM-CCD is 0.5 ms.

2.4.2. Raman point analysis

Point measurements used a 532 nm laser and a 100x objective (Olympus, NA 0.9) for analysis of wafers and thin sections in case studies 1 and 2 (sections 4.1.2 and 4.2.3), respectively. Accordingly, the laser spot size is of less than 1.5 µm ($d = 1.22\lambda/NA$) in the X-Y plane for all cases, and due to the confocal setting, the axial resolution is less than 3 µm ($dz = 1.4\lambda/NA^2$)[51]. A spectral window of 100 to 4000 cm^{-1} was

selected in combination with a 150 grooves/mm grating, and spectra were acquired with two accumulations of 15 s each in the same spot. Measurements used a confocal pinhole aperture of 50 μm in the case of thin sections or 100 μm for wafers. The spectral resolution is here defined as the measured FWHM of two Ne emission lines at 585.25 nm and 837.76 nm, respectively, for which the line width is far lower than the instrumental resolution. The 150 grooves/mm grating with the 50 μm pinhole provides a spectral resolution of 8.8 cm^{-1} at 585.25 nm and 4.5 cm^{-1} at 837.76 nm. While with the 100 μm pinhole, spectral resolutions of 12.2 cm^{-1} and 6.1 cm^{-1}, respectively, are achieved.

For analyses of the OH vibration modes, which required high spectral resolution (see case study 1; section 4.1), the 1800 grooves/mm grating was used. In this case, the acquisition time was increased to two accumulations of 30s each, the confocal pinhole was set to 100 μm, and the grating was centered on the desired peak position (~3350 cm^{-1}). The spectral resolution for this setting is 1.1 cm^{-1} and 0.44 cm^{-1} at 585.25 nm and 837.76 nm, respectively.

2.4.3. Raman mapping

Photomicrograph mosaics were used as basemaps for mapping spatial reference. Mapping analyses used the 50x long-working distance objective. The Horiba SWIFT® technology was applied to decrease the total mapping time. It relies on a trigger-communication between the XYZ stage and the CCD detector, which continuously moves the stage in the X-direction while irradiating the sample, designing a line-scan mapping array. The signal is processed only after a full line scan has been completed, thus substantially decreasing the readout time when compared to point-scan mapping.

Mapping settings intended to maximize the signal quality and area coverage while minimizing the total mapping time. Considering that each Raman map covered different minerals and areas, the settings requirement of each map was also variable. The large area map of case study 1 (section 4.1) was analyzed using the Horiba DuoScan®, which scanned the laser over an area of 20x20 μm (macropixel) and generated an average spectrum of this region. This technology allows the acquisition of large maps without creating blank or interpolated spots between the analysis points. In case study 1, analytical conditions were 0.5 s single accumulation, 1800 grooves/mm grating with the spectrometer centered around 3350 cm^{-1} (range 3188 to 3505 cm^{-1}), 532nm laser, 100% filter, 100μm confocal pinhole, detector EM gain of 700, 20 μm step on the X and Y directions. The focus was automatically checked at the start of each line by an autofocus feature. A total of 71051 points were analyzed in an area of 4.54 mm x 6.26 mm (28.42 mm^2) for a duration of 10 hours and 37 minutes. For the second case study (section 4.2), measurements consisted of 0.3 s single accumulations, arranged in a regular 8 x 8 μm array. Conditions were set as EM gain 300, 532 nm laser, 25% filter, 50 μm confocal pinhole, 150 grooves/mm grating, and a range from 50 to 4000 cm^{-1}. A total of 6348 points were analyzed in an area of 0.552 mm x 0.736 mm (0.406 mm^2) for a duration of 36 minutes and 04 seconds.

The laser depth penetration in the samples for the mapping acquisition settings is estimated at around 3 µm (dz (radius) ~ 4.4 nλ / 2πNA^2)[52]. However, the exact value can vary slightly between each phase depending on the interaction of the crystal with the laser, since mineral properties (*i.e.* color, refractive indices, crystal orientation, etc.) are known to affect this interaction[35,53].

A summary of the analytical conditions used for the acquisition of each dataset in this study is presented in Table 1.

Table 1: Analytical conditions used in the acquisition of each dataset for the case studies and their respective images in the manuscript.

	Dataset	Objective (magnification)	Laser (nm)	Laser power	Grating (grooves/ mm)	Confocal pinhole (µm)	Acquisition time (s x accumulations)	Obs.	Images
Case study 1 (amblygonite -montebrasite sample)	Point analyses	100x	532	100%	150	100	15 s x 2		Figure 2A and B
					1800	100	30 s x 2		Figure 2C and D
	Mapping	50x	532	100%	1800	100	0.5 s x 1	SWIFT mode and DuoScan	Figure 3
Case study 2 (complex phosphate assemblage)	Point analyses	100x	532	25%	150	50	15 s x 2		Figure 4
	Mapping	50x	532	25%	150	50	0.3 s x 1	SWIFT mode	Figure 5

2.4.4. Calibration and data processing

Spectra were acquired and treated with the LabSpec 6.5.2 software. Spectrometer X-axis calibration (Raman shift) was performed daily using the NIST certified Horiba SP-RCO objective (polystyrene Raman peak at 1001.4 cm^{-1}), and cross-checked with a silicon standard (Raman peak at 520.2 ± 0.5 cm^{-1} [54]). Y-axis calibration (intensity) was done with an intensity correction curve based on the white light irradiance spectrum of a NIST certified Avantes AvaLight-HAL-CAL-Mini source. A spike filter was applied automatically during analysis by comparing multiple accumulations and removing spikes that did not repeat. Visible and hidden peaks were fitted using the PeakFit, v.4.12, from SYSTAT Inc. Fitting followed the automated procedure using residuals, including a linear or quadratic baseline fitting, and Gaussian+Lorentz (amplitude model) parameters. Fitting procedures focused to maximize the coefficient of determination (r^2) and the F-statistic values while minimizing the fit standard error (SE). The Spectragryph software, version 1.2 by Dr. Friedrich Menges, was also used for spectra visualization.

Point analyses were only subjected to baseline corrections. In case study 1, full-range spectra acquired with the 150 grooves/mm grating had an 8-degree polynomial baseline subtraction with 150 attaching points, while the analyses of the OH vibration region with the 1800 grooves/mm grating had a 2-degree polynomial baseline subtraction also with 150 points. Case study 2 had a 6-degree polynomial baseline correction with 150 attaching points, except for the spectra of samuelsonite and quartz, which had an 8-degree polynomial baseline subtraction with 150 attaching points.

When dealing with very low acquisition times (*i.e.* less than one second), such as in the case of Raman mapping, the signal-to-noise (S/N) ratio can be small. This requires an additional step of data processing to improve the signal and facilitate the analysis of both measured points and resulting images. Likewise, studies show that for hyperspectral images, such as Raman maps, it is mandatory to have some pre-processing of spectral data[55]. However, no universal processing procedure can be proposed, being highly dependent on the specific acquisition settings of each map and what type of information they provide. The specific processing parameters used in this study were selected after a comparison of several treatment trials, in which the parameters that provided the best S/N without compromising any spectral feature were chosen.

In this study, two areas were mapped, each corresponding to one of the case studies in the following results section. Data processing typically consisted of selecting a relevant spectral range, applying a baseline correction, and removing analyses that reached the detector saturation. However, each map had its specific processing settings which are presented below. For the first case study, the processing steps consisted of a second-order polynomial baseline subtraction with 40 attaching points and 30 noise correction points, second-order Savitzky–Golay polynomial smoothing, and removal of the photoluminescence signal above 500 counts from 3200 to 3320 cm^{-1} and in the 3400 to 3450 cm^{-1} range, where no Raman peaks were present. In the second case study, processing steps included removal of the signal that reached the detector saturation above 30000 counts in the range between 0 and 1500 cm^{-1}, a 7-degree polynomial baseline subtraction with 25 attaching points and 15 noise correction points, a range reduction retaining only data between 400 and 3650 cm^{-1}, and a second 12-degree polynomial baseline subtraction with 165 attaching points to fit the spectra into a lower background level.

The Savitsky-Golay smoothing was applied in the mapping dataset due to the short acquisition times (0.5s or lower), which imposed a low signal-to-noise ratio to the spectra. The smoothing procedure was required to improve the classification with the multivariate algorithms.

In the mapping datasets, where multiple analyses at the same spot using more than one laser wavelength were not performed, whenever the spectra background baseline had higher intensity than the Raman peaks the signal was interpreted as broad photoluminescence emissions (cf. Nasdala et al.[35]). Furthermore, whenever a signal reaches the detector saturation it should be removed from the dataset and not be used in multivariate statistical analyses because there is no guarantee that the signal is complete. It could be that part of the signal was lost because the detector was already saturated, and this will affect the dataset classification. The raw and processed spectra for each processing step are available in the supplementary files (Figures S1 and S2).

To compare the effects of spectral processing on the Raman images, the second case study was also processed with fewer steps, comprising only the removal of points that reached the detector saturation, and subtraction of a 7-degree polynomial baseline with 25 attaching points and 15 noise correction points.

All Raman images presented in this manuscript were XY smoothed to improve the visualization of mineral contacts and to remove rastering effects.

Calculation of the F content in the amblygonite-montebrasite sample of case study 1 used the formula F[mass%] = 0.0847 * FWHM[cm^{-1}] - 0.4053 of Hulsbosch and Muchez[49], which is an improved form of the calculations from Rondeau et al.[32]. The conversion from mass% to mol% considered the molar proportions of the ideal formulas of both end-members ($LiAlPO_4F$ and $LiAlPO_4OH$) and that the only chemical substitution in the system is the exchange of F and OH.

2.4.5. Multivariate statistical analysis (MVA)

Multivariate statistical analyses were performed with the LabSpec MVA plus module. Classical least squares (CLS) fitting, principal components analysis (PCA), and multivariate curve resolution (MCR) algorithms were applied to process the Raman maps. The supervised CLS method allows the user to select reference spectra as inputs to classify the dataset. The algorithm compares all measured spectra with the selected references, and assign each spectrum of the dataset to the most similar reference. This procedure can be done for an unlimited number of phases but depends on the user to know if the final image corresponds to its previous assessment. In this study, seven reference spectra were selected from the treated dataset as inputs in the supervised CLS algorithm. This selection was based on the number of phases observed during preparatory optical and Raman point analyses. To decrease the influence of the user's choice in the reference spectra, references were defined using an area selection instead of single points. The selected areas were based on previous point analyses and showed homogeneous Raman signal.

For the unsupervised PCA methods, the user sets the number of components (or a maximum number), and the algorithm classifies all measured spectra into the defined number of components. These components are ranked according to the variance within the dataset (*i.e.* first component corresponds to the highest variance and the last to the lowest). It should be noted that the output components do not represent any true chemical composition and thus are problematic to interpret and cannot be compared with references. In the unsupervised MCR method, the user can also set the number of components, and the measured spectra are classified into the defined number of components. In comparison to PCA, the MCR algorithm can be slower for analysis of large datasets (>10000 spectra), and the components are not ranked in any way, but the output components do resemble ideal chemical compositions within the dataset, which can then be compared with reference databases. In this study, the unsupervised PCA and MCR methods were based on automated classification of the treated dataset into six components and included an area normalization pre-processing step, followed by score normalization after classification. The algorithms of both PCA and MCR

demonstrated a maximum detection of six components in the sample, any additional components only accounted for noise in the dataset without the selection of extra phases. The loadings obtained by each MVA algorithm are available in the supplementary files (Figures S1 and S2).

3. BACKGROUND INFORMATION

3.1. Raman signature of phosphate minerals

Before going into the study of molecular vibrations of phosphate minerals for mineral identification and paragenetic studies, it is important to take into account their molecular structure and represent phosphates in a hierarchical mineral classification. During the crystallization of complex rock systems such as pegmatites, mineral changes are mainly represented by modifications in the crystal structure rather than by chemical changes[56]. Thus, complex minerals respond to changing P-T-X conditions by adapting their crystal structure and by recrystallizing into different phases. Consequently, classifications based on the molecular structure of minerals are preferred for complex mineral systems, posing a framework to understand the behavior of minerals in geological processes and their paragenetic sequence[56]. An initial condition for the molecular structure classification of phosphate minerals is that they cannot be classified in the same way as silicate minerals[3,56–58], that is, by the polymerization of the main oxyanion, $[SiO_4]^{4-}$ in the case of silicates and $[PO_4]^{3-}$ for phosphates. Pauling's second rule and the valence-sum rule[59] state that for a given atom the sum of its bond-valences should be equal to or less than its formal valence. As phosphorus has a 5+ charge and occurs in tetrahedral coordination with oxygen, the mean bond-valence (ion charge/coordination number) to each oxygen atom in the $[PO_4]^{3-}$ oxyanion is 5/4 or 1.25 valence unit (vu). Consequently, two $[PO_4]^{3-}$ tetrahedra rarely polymerize by themselves, since the bridging oxygen atoms would receive 2.5 vu, disobeying the valence-sum rule. The polymerization in phosphate minerals thus requires additional groups where the ligand anion (ϕ = oxygen, hydroxyl, fluorine, etc.) bond-valence is $\leq$ 0.75 vu, such as higher-coordination number groups or other tetrahedral coordinated groups[3,56,58]. These initial clusters of $[PO_4]^{3-}$ tetrahedron connected to other polyhedra are regarded as the fundamental building blocks of the phosphate mineral crystal structure, which when repeated in a regular array constitute the structural unit[56,58]. The structural unit, in turn, is interconnected by an interstitial unit, usually composed of large cations. A side note on polymerized [P-O-P] structures is required here. These structures do exist as condensed phosphates (*e.g.* pyrophosphate, polyphosphates, and metaphosphates) in biological and synthetic systems[60,61], but are uncommon in geological materials[58]. Our reasoning follows the premise of Huminicki and Hawthorne[58], where the rare occurrence of polymerized [P-O-P] structures allows the description of natural phosphate minerals as not polymerized by the $[PO_4]^{3-}$ oxyanion. A full discussion on the occurrence of condensed phosphates is outside the scope of this manuscript.

Many classification schemes proposed for phosphate minerals have been based on the polymerization of the structural unit and on the nature of cations that make up the interstitial unit[5,56–58,62]. The most recent classification of Huminicki and Hawthorne[58] arranged phosphate minerals according to which polyhedra polymerize to form the structural unit. The $[PO_4]^{3-}$ tetrahedron can be linked to: (1) another tetrahedron ($[BeO_4]$, $[ZnO_4]$, and $[AlO_4]$); (2) an octahedron ($[AlO_6]$,$[FeO_6]$,$[MnO_6]$); or (3) large-cation polyhedra with coordination number higher than six (*e.g.* Na, Ca, U, and rare earth elements). Additionally, each of those groups is subdivided by the mode of polymerization of the structural unit into: (a) unconnected polyhedra, (b) finite clusters, (c) chains, (d) sheets, and (e) frameworks.

Structural classifications of phosphate minerals, when experimentally calibrated, provide the framework to correlate the mineralogical evolution of complex assemblages with the P-T-X evolution of the crystallization medium. In the case of phosphates in magmatic systems, their paragenesis should reflect the distinction between 1) primary minerals, crystallized directly from the magma; 2) hydrothermal minerals formed by the interaction of primary minerals with high-temperature magmatic-hydrothermal fluids, or directly precipitated from these fluids; and 3) supergene minerals crystallizing from the interaction of previous minerals with low-temperature shallow waters under surface conditions (Figure 1). Hawthorne[56] demonstrates that some minerals, especially in the framework phosphates, can show a deviation from the perfect valence bond. These non-ideal bonds can be stabilized at high temperatures due to the larger thermal displacements in the crystal structure, but as temperature decreases, the displacement is reduced and the framework structure tends to disrupt, being progressively replaced by sheet structures, chain structures, etc. The concomitant increase in the activities of [OH] and $[H_2O]$ groups may enhance this destabilization process, as they link with the structural unit and inhibit its polymerization. Consequently, the role of H in the mineral structure is of great importance, as it controls the dimensionality of the structural unit and tends to break down the polymerization degree, creating increasingly isolated structures (low-polymerization) as H increases in content[56].

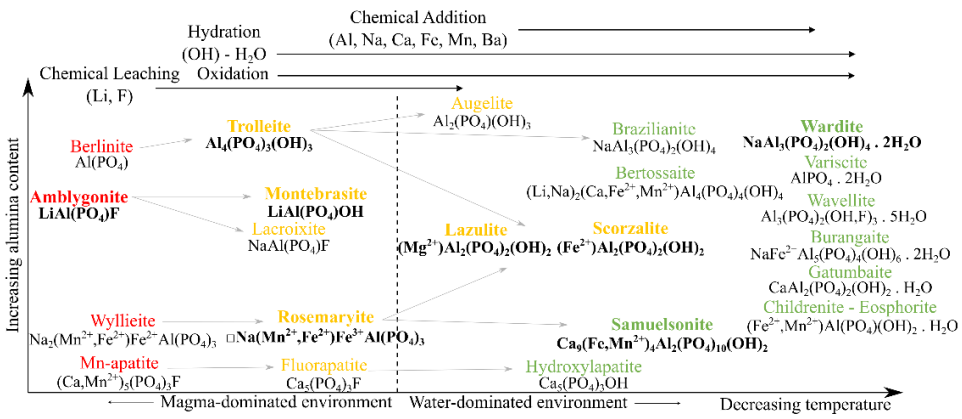

Figure 1: Sequencing of some phosphate minerals from the Buranga pegmatite with decreasing temperature. The vertical axis represents the content of Al_2O_3 in the mineral formula and the horizontal axis represents temperature. Phosphates are separated into three domains: magmatic to the left, colored in red; magmatic-hydrothermal in the center, colored in yellow; and low-temperature hydrothermal-supergene to the right, colored in green. Grey arrows indicate possible direct sequential relations. The mineral list is a part of the phosphates described in the Buranga pegmatite[36,39]. The placement of minerals in the diagram is based on natural observations of mineral relations [4,25,38,39,63], experimental determinations of mineral stability[20–22,64], and modified according to the author's observations.

Raman spectroscopy fits naturally with the structural classification of phosphates, as the analysis of a mineral's vibration helps to investigate its molecular structure. The Raman spectra of minerals is mostly a reflection of the core anionic part, or structural unit, and its polymerization degree. Therefore, changes in the structural unit are easily recognized with Raman analyses.

A compilation of Raman data from the literature and respective band assignments for phosphate minerals is presented in the supplementary files (Table S1). The free phosphate tetrahedron has four normal vibrational modes (Table 2): a singly degenerate symmetric stretching (A_1) of wavenumber 938 cm^{-1}, a doubly degenerate symmetric bending (E) of wavenumber 420 cm^{-1}, a triply degenerate asymmetric stretching (F_2) at 1017 cm^{-1}, and a triply degenerate asymmetric bending (F_2) at 567 cm^{-1} [65]. These normal modes are assigned as ν_1, ν_2, ν_3, and ν_4, respectively[65]. As the tetrahedral phosphate group is embedded into a crystal structure, its symmetry can be lowered, partly lifting the degeneracy of the normal modes and consequently, splitting the vibrational bands into separate components[66,67]. The polymerization with other polyhedral units can also drive some anionic groups to occupy different structural sites within the crystal structure, causing further splitting of vibrational bands. Additionally, new modes can also indicate impurities in the mineral composition, which cause local deformations in the crystal structure[66,67]. In essence, minerals of higher symmetry and simpler composition will show fewer peaks and be easily correlated with the free tetrahedral phosphate group. Minerals of lower symmetry or with complex composition will show an increased number of peaks that deviate from the original phosphate group vibrations. A clear example is the occurrence of hydroxyl and molecular water groups within the structure, which not only breaks the polymerization of the structural unit, creating different peaks of the main anionic group but also provides additional peaks by their internal vibrational modes[62].

Table 2: Band positions (in cm^{-1}) of main vibrations of the free $[PO_4]^{3-}$ unit.

ν_2 (E - R)	ν_4 ($F_2^{(1)}$ - R,IR)	ν_1 (A_1 - R)	ν_3 ($F_2^{(2)}$ - R,IR)	Ref.
363	515	980	1082	Ross[62]
358	500	970	1080	Ross[62]
420	567	938	1017	Ross[62]
420	567	938	1017	Griffith[65]
420	564	938	1009	Jastrzebski et al.[68]
420	562	937	1022	Jastrzebski et al.[68]

R = Raman active vibrations, IR = infrared active vibrations
A_1 = singly degenerate symmetric stretching, E = doubly degenerate symmetric bending
$F_2^{(2)}$ = triply degenerate asymmetric stretching, $F_2^{(1)}$ = triply degenerate asymmetric bending

Spectra of phosphate minerals can be divided into three domains: 1) high wavenumber region (1300-4000 cm^{-1}) representing vibrations of water and hydroxyl molecules; 2) medium wavenumber region (250-1300 cm^{-1}) representing vibrations of the oxyanions from the structural unit; and 3) low wavenumber region (<250 cm^{-1}), usually related with crystalline lattice modes or cation-oxygen modes of the interstitial unit[65].

Main vibrations of minerals observed were assigned after comparison with published data (Table 2 and Table S1). The phosphate group [PO_4] modes in the crystalline structures are largely represented by an in-plane bending (ν_2) from 350 to 500 cm^{-1}, an out-of-plane bending (ν_4) from 500 to 650 cm^{-1}, a symmetric stretching (ν_1) from 930 to 1000 cm^{-1}, and an asymmetric stretching (ν_3) from 1000 to 1150 cm^{-1} [32,33,42,62,66–69]. Stretching vibrations of the [AlO_6] octahedron are found from 600 to 680 cm^{-1} [38,62,69] and around 700 to 900 cm^{-1} for [AlO_4] tetrahedron[62]. The H_2O molecule stretching vibrations occur from 3000 to 3400 cm^{-1} and bending from 1600 to 1700 cm^{-1} [62]. The OH group normal modes usually occur at high wavenumbers, and are represented by a stretching vibration of the molecule from 3300 to 3600 cm^{-1} [32,42,62] and bending vibrations at 800-830 cm^{-1} and 1187 cm^{-1} [42,69]. The assignment of bands below 500 cm^{-1} is most difficult as several vibrations of [MO_6], [AlO_n], [PO_4], and lattice vibrations can be superimposed in this region, with many conflicting assignments in literature[42,62,69].

Band assignment is important to understand how molecular changes are reflected in the crystal structure, and consequently in the Raman spectrum. For example, the Raman spectra of the amblygonite[$LiAl(PO_4)F$]–montebrasite[$LiAl(PO_4)OH$] solid solution series are similar in the number of peaks and general shape, but important shifts occur in three specific regions[32], at about 600 cm^{-1} (P4 in Figure 2), 1060 cm^{-1} (P8 in Figure 2), and 3375 cm^{-1} (P10 in Figure 2). Only the region at 3375 cm^{-1} can be unambiguously assigned to the OH-stretching vibration, which varies continuously from around 3348 cm^{-1} in amblygonite to 3379 cm^{-1} in montebrasite[32]. Additionally, this shift in the νOH peak position (P10) is accompanied by an increase in peak FWHM with increasing F content[32]. The OH-stretching band can thus be used to easily distinguish between the two end-members of the series, and is the most accurate way to quantify the F/OH ratio of the sample[32,49].

3.2. Rationale of case studies

3.2.1. Case study 1: Amblygonite-Montebrasite Sequence

The studied sample represents an occurrence of Al-phosphates of the amblygonite [Amb = $LiAl(PO_4)F$]-montebrasite [Mbs = $LiAl(PO_4)(OH)$] solid-solution series from the Buranga pegmatite. The series has a mixed octahedral-tetrahedral framework structural unit composed of [PO_4] tetrahedra cross-linking corner-sharing octahedral chains [AlO_5], where F and OH act as ligands. The interstitial unit is represented by Li cations in a distorted octahedral arrangement[70]. The mineralogical distinction of these two phases is not straightforward, as both amblygonite and montebrasite share most optical and physical properties[71]. In hand specimens, both are colorless, whitish, greyish, or yellowish, show a white streak, and have Mohs hardness around 5.5 to 6. Under transmitted light, they are colorless to whitish, non-pleochroic, biaxial negative, have three main cleavage directions, and have moderate relief. Their crystallographic features are also similar, both minerals are from the triclinic system, point group $\bar{1}$, space group $C\bar{1}$. They do have differences, such as density contrast (3.04-3.11 g/cm^3 and 2.98-3.04 g/cm^3, for amblygonite and

montebrasite respectively), 2V angle (107-129.5˚ and 66-101˚, respectively), birefringence (0.020 and 0.026), and refraction indices (nα = 1.577-1.591, nβ = 1.592-1.605, nγ = 1.596-1.613, and nα = 1.594-1.615, nβ = 1.608-1.624, nγ = 1.616-1.646, for amblygonite and montebrasite respectively). However, these characteristics are not always easy to measure. Moreover, chemical mapping of the spatial and paragenetic replacement reactions of amblygonite is also problematic as most micro-analyses are based on electron beam bombardment (SEM, EPMA, etc.) and amblygonite-montebrasite exhibits sensitivity to electron beam irradiation causing significant errors on the fluorine determination[13].

The distinction between amblygonite and montebrasite has previously relied on different techniques such as: optical indexes[72], X-ray crystal diffraction[73], and infrared spectroscopy[42]. Recent studies have shown that Raman spectroscopy can be used to distinguish amblygonite from montebrasite, and also estimate their F contents[32]. Currently, considering the advances in Raman spectroscopy instrumentation presented in the methods section 2.4.1, the analysis time required to distinguish these phases is strongly decreased to the order of few seconds per analysis, opening the possibility to visualize their spatial relationships and to investigate their formation processes.

This study uses the classification of the amblygonite-montebrasite series according to the molar amount of Amb (*i.e.* $LiAl(PO_4)F$) in the solid-solution mineral formula $[LiAl(PO_4)(F,OH)]$ (cf. [74]). A sample with F/(F+OH) ratio of 1 (F content of 12.85 mass% or 12.5 mole%,) represents the pure amblygonite endmember with Amb_{100} (100% amblygonite and 0% montebrasite). A sample with F/(F+OH) ratio of 0.5 (F content of 6.425 mass% or 6.25 mole%) represents an intermediate composition Amb_{50} (50% amblygonite and 50% montebrasite), and marks the division between the two sides of the solid-solution. A sample with F/(F+OH) ratio of 0 (0% F) represents the pure montebrasite endmember with Amb_0 (0% amblygonite and 100% montebrasite). Additionally, for the purpose of this study, four compositional intervals are defined as: F-poor montebrasite (Amb_{0-25}), F-moderate montebrasite (Amb_{25-40}), F-rich montebrasite (Amb_{40-50}), and amblygonite (Amb_{50-100}). Further subdivision of amblygonite samples is not required because natural occurrences of F-dominated samples (F/(F+OH) > 0.65, or $Amb_{>65}$) are uncommon[70,75], especially for pegmatitic samples[13,76].

3.2.2. Case study 2: Mineral reactions in phosphate assemblages

In case study 1, Raman mapping was applied to investigate the mineralogical and spatial extent of replacement relations between two Al-phosphate species belonging to a solid solution series. Case study 2 goes one step further and investigates the textural relations in a complex assemblage composed of multiple phosphate minerals. Many of these phosphates have complex chemistry and structure defined by the presence of OH groups or molecular water, crystallographic vacancies, and Fe and Mn in multiple oxidation states. Consequently, routine high spatial resolution identification of phosphates by electron beam techniques is not straightforward[77].

4. RESULTS

4.1. Case study 1: Amblygonite-Montebrasite Sequence

4.1.1. Optical analysis

In hand specimen (Figure 3a), the sample shows a transition from transparent greenish tints to translucent or opaque whitish regions. Under transmitted light, the transparent greenish region demonstrates a much higher crystallinity, while the translucent to opaque alteration region is composed of a more polycrystalline matrix which is spatially concentrated in microfractures and cleavage planes of the transparent region (Figure 3a). Optical properties of the pristine transparent region are: colorless, non-pleochroic, three cleavage directions, low birefringence, and biaxial negative optical sign, supporting its identification as a member of the amblygonite-montebrasite series. However, the exact distinction cannot be confidently made under the optical microscope. Additionally, the characterization of the translucent to opaque regions is even harder due to their poor visibility and difficulty to define optical properties.

4.1.2. Raman analysis

Figure 2 shows that the Raman spectra of the translucent and transparent regions, even though mostly similar, have some distinctions between them, especially the position and shape of the OH-stretching peak (P10). In the translucent to opaque region (point A in Figure 3a), the OH-stretching peak is positioned at 3375 cm^{-1} with a FWHM of 20.6 cm^{-1}, closely related to a F-poor phase[32]. In contrast, in the transparent region (point B in Figure 3a) the peak is positioned at 3349 cm^{-1} and has a FWHM of 53.8 cm^{-1}, similar to a F-enriched phase[32].

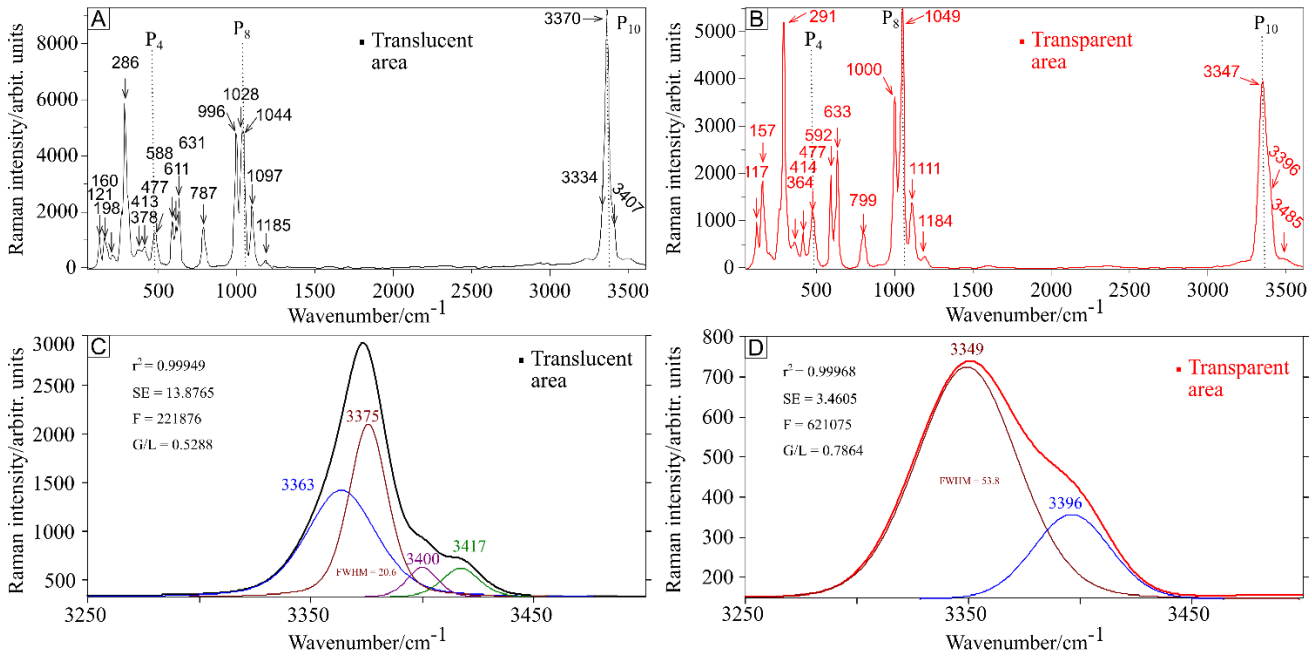

Figure 2: Raman spectra from the amblygonite-montebrasite sample of Buranga showing the distinction of peak positions between the translucent and transparent regions, related to the points A and B of Figure 3, respectively. **A)** Full range spectra acquired with the 150 grooves/mm grating. Peak numbering (*i.e.* P4, P8, and P10) according to Rondeau et al.[32]. **B)** Raman spectra of the OH-stretching vibration region (P10) acquired with the 1800 grooves/mm grating for both the translucent and transparent areas. **C)** and **D)** OH-stretching region for the translucent (C) and transparent (D) areas with respective fitted peaks and fitting parameters. Fitting parameters are represented by r^2 (coefficient of determination), SE (fit standard error), and F (F-statistic). G/L notation represents the Gaussian/Lorentzian ratio of fitted peaks.

Even though point analyses can easily separate amblygonite from montebrasite, to fully characterize all minerals present and investigate the spatial distribution of the alteration process, a Raman mapping experiment is performed. The maps of peak position and FWHM of the P10 are shown in Figure 3b and c, respectively. Based on these images, three Raman zones can be identified. Firstly, a zone with peak positions from 3350 to 3360 cm^{-1} and FWHM from 70 to 85 cm^{-1} is observed in the top right portion of the sample, equivalent to the transparent region in the optical photomicrograph. Secondly, a zone with peak positions from 3370 to 3380 cm^{-1} and FWHM from 25 to 45 cm^{-1}, is observed mostly in fractures and restricted to the lower part of the sample where the translucent to opaque region occurs. Thirdly, a transitional zone between the two previous zones has peak positions from 3360 to 3370 cm^{-1} and FWHM from 45 to 70 cm^{-1}. These spectral properties, especially the FWHM, are sensitive to the amount of fluorine and thus, can be used to estimate the fluorine content of the mineral phase[32,49]. Figure 3c shows the estimated fluorine distribution in the sample after applying the formula F[mass%] = 0.0847 * FWHM[cm^{-1}] - 0.4053 of Hulsbosch and Muchez[49] to the mapping dataset. The Buranga sample has fluorine contents ranging from 1.7 to 6.6 mol%. Considering the optical regions, the transparent region has a fluorine content from 5.4 to 6.6 mol%, corresponding to a F-rich montebrasite with mineral proportions of Amb_{40} to $Amb_{50,}$ while the translucent to opaque region contains 1.7 to 3.3 mol% fluorine, representing a F-poor montebrasite with Amb_{10} to Amb_{25} proportions. The transitional zone has intermediate values between the previous two, classifying as a F-moderate montebrasite.

The three zones become spatially explicit by applying multivariate analysis such as the classical least squares (CLS) method. This analysis is one way to separate into discrete zones (*e.g.* mineral zones) what is a rather continuous process (*e.g.* mineral replacement), allowing the spatial visualization and quantification of these zones, and highlighting their textural relations. Figure 3D shows that the F-rich montebrasite (Amb_{40-50}) covers 36% of the map area in the top and central regions. It is fairly corroded and irregular, with most fractures and cleavage planes being replaced by the F-moderate montebrasite (Amb_{25-40}), which in turn occupies 56% of the map area. The F-poor montebrasite (Amb_{10-25}) corresponds to the strongly altered opaque regions and covers 8% of the map, mostly comprising the internal part of broad fractures.

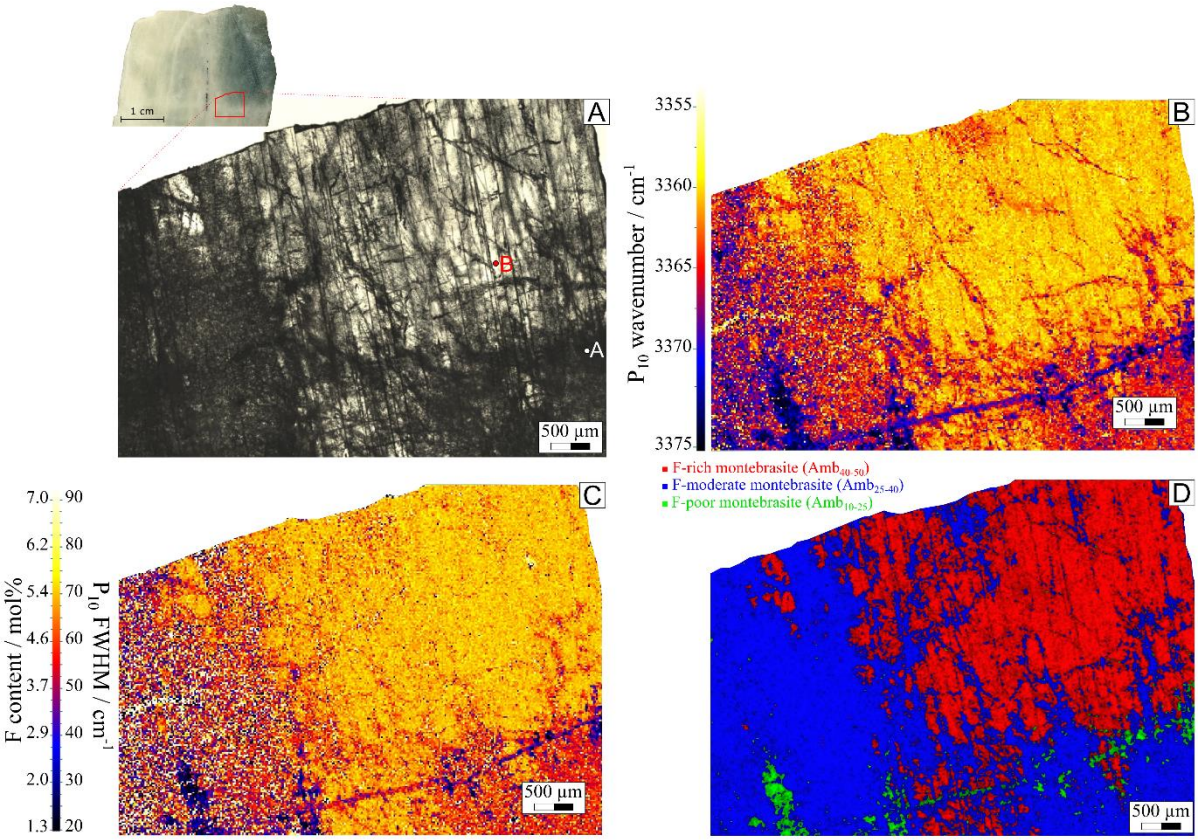

Figure 3: Case study 1 Raman mapping of the amblygonite-montebrasite sample from the Buranga pegmatite. **A)** Optical photomicrograph mosaic obtained under transmitted white light with 5x objective and parallel polarizers. The transparent region is the colorless area and translucent to opaque regions are represented by dark patches of poor visibility. A and B mark the location of point analysis in Figure 2. Straight subvertical lines and diagonal top left to bottom right lines are cleavage planes. The top-left inset is a picture of the full sample in hand specimen (BU18FA09). **B)** OH-stretching vibration (P10) peak position (wavenumber/cm^{-1}) Raman map. White pixels represent spectra that were removed from the dataset because their signal reached the detector saturation. **C)** OH-stretching vibration (P10) peak FWHM (cm^{-1}) Raman map and calculated fluorine content distribution (mol%). Fluorine content estimation is based on the equation F[mass%] = 0.0847 * FWHM[cm^{-1}] - 0.4053 of Hulsbosch and Muchez[49]. White pixels represent spectra that were removed from the dataset because their signal reached the detector saturation. **D)** CLS algorithm output map from the mapping dataset of the amblygonite-montebrasite sample from the Buranga pegmatite.

4.2. Case study 2: Mineral reactions in phosphate assemblages

4.2.1. Optical analysis

The sample consists of a bluish phosphatic nodule with dark-colored minerals inside and surrounded by a cream-colored cap (Figure S3a in supplementary files). Unambiguous identification of most of these phases solely by optical characteristics is very hard. Some phases can be suggested at this stage, but require further confirmation by other analysis, such as Raman spectroscopy. The transparent, light blue to colorless, non-pleochroic, and biaxial (-) mineral, with medium birefringence and moderate relief, suggests trolleite [$Al_4(PO_4)_3(OH)_3$]; the dark blue traces of a translucent, strongly pleochroic, and biaxial (-) mineral with high birefringence, one distinct cleavage direction, and moderate relief indicates the presence of scorzalite-lazulite [$(Fe,Mg)Al_2(PO_4)_2(OH)_2$]; the transparent, light pink to colorless, non-pleochroic, and biaxial (-) mineral with low-medium birefringence, one good cleavage direction, and high relief points to bertossaite [$(Li,Na)_2(Ca,Fe,Mn)Al_4(PO_4)_4(OH)_4$]; the translucent, brown, non-pleochroic, and biaxial (+) mineral with high birrefringence, one good cleavage direction, and high relief can be rosemaryite

[□Na(Mn,Fe)Fe^{3+}Al$(PO_4)_3$]; and the transparent, creamy, non-pleochroic, and biaxial (+) mineral with medium birefringence, one good cleavage direction, and moderate relief points to brazilianite [$NaAl_3(PO_4)_2(OH)_4$]. Nevertheless, considering only the optical properties, identifications should be regarded as hypotheses of possible major minerals.

Textural analysis under transmitted light shows altered crystals of brownish subhedral rosemaryite surrounded by colorless subhedral trolleite and colorless anhedral quartz. Between rosemaryite and trolleite occurs an anhedral dark-blue scorzalite-lazulite (Figure 4a). Other accessories phases are visible under the optical microscope, but due to their size and shapes, optical properties are hard to observe and, consequently, mineralogical identification is even more difficult.

4.2.2. Energy-dispersive X-ray spectroscopy

To characterize the chemistry of those phases, the sample was analyzed with the electron microscope. EDS maps show the distribution of some major elements in the area (Figure S3b in supplementary files). An Al-rich area surrounds a Mn-rich mineral, which in turn has its fractures filled by a Ca-rich phase, and shows a Mg-rich tip. Additionally, a Si-rich mineral is highlighted between the many phosphates.

Just by the chemical distribution of elements, it is still problematic to uniquely identify the phases observed, as many phosphates share the same chemical compounds highlighted in the images. For example, both trolleite [$Al_4(PO_4)_3(OH)_3$] and montebrasite [$LiAl(PO_4)(OH)$] could be the bright phase in the Al-map, and they have the same chemical characteristics in every other map. This demonstrates that straightforward determination of complex phosphate phases is not possible by EDS or other electron beam techniques.

4.2.3. Raman analysis

Contrarily to the optical and EDS analyses exposed previously, Raman spectroscopy can distinguish all phases present in the mapping area. In total, seven minerals are recognized with Raman analyses, each showing unique spectral features (Figure 4). Firstly, major phases observed in the optical microscope, can now be unambiguously identified as: (1) trolleite, marked by a strong OH-stretching vibration around 3436 cm^{-1} accompanied by a smaller side peak at 3518 cm^{-1}, it has [PO_4] tetrahedron vibrations at 476 (ν_2), 609 and 632 (ν_4), 987 (ν_1), 1072 and 1109 (ν_3) cm^{-1}; (2) rosemaryite has [PO_4] main vibrations at 483 ($_{\nu 2}$), 592 (ν_4), 993 (ν_1), and 1117 (ν_3) cm^{-1}; and (3) quartz, marked by a strong O-Si-O bending vibration at 461 cm^{-1}. Secondly, the occurrence of the scorzalite-lazulite series is not only confirmed, but a distinction between the (4) Mg-rich end-member lazulite and the (5) Fe-rich scorzalite is possible. Lazulite has a strong [PO_4] tetrahedron ν_3 vibration at 1044 cm^{-1} surrounded by smaller peaks at 1006, 1086, and 1130 cm^{-1}, and has a sharp OH-stretching vibration around 3370 cm^{-1} and FWHM of 20 cm^{-1}. Scorzalite has a strong [PO_4] ν_3 vibration at 1046 cm^{-1} surrounded by smaller peaks at 1010, 1059, and 1115 cm^{-1}, and has a broader OH-stretching vibration around 3388 cm^{-1} with FWHM of 36 cm^{-1}. Lazulite occurs spatially close to rosemaryite, while scorzalite is associated with trolleite. Lastly, the accessory phases which could not be

identified with the optical and EDS analyses are successfully characterized as: (6) samuelsonite [$Ca_9(Fe,Mn)_4Al_{12}(PO_4)_{10}(OH)_2$], which occurs in fractures and surrounding rosemaryite, and has [PO_4] vibrations at 412 and 441 (ν_2), 558 and 573 (ν_4), 957 and 983 (ν_1), 1013 and 1066 (ν_3) cm^{-1}; and (7) wardite [$NaAl_3(PO_4)_2(OH)_4 \cdot 2H_2O$], which is associated with scorzalite in the rims of trolleite, and has [PO_4] vibrations at 465 and 482 (ν_2), 593 and 617 (ν_4), 992 (ν_1), 1047, 1077 and 1101 (ν_3) cm^{-1}.

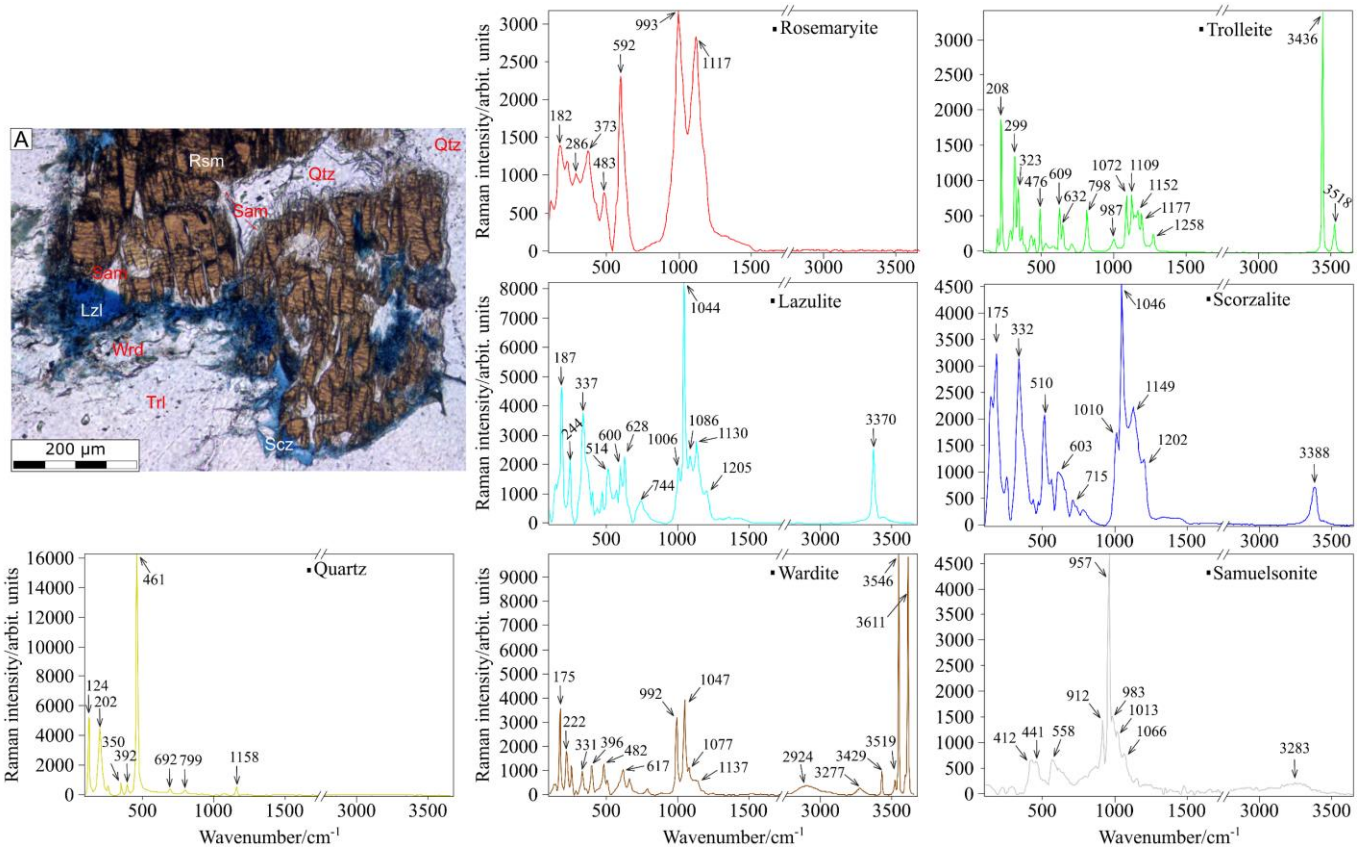

Figure 4: Case study 2 complex phosphatic assemblage from the Buranga pegmatite. **A)** Optical photomicrograph of the assemblage obtained with a 10x microscope objective under transmitted light and parallel polarizers. Lzl = lazulite, Qtz = quartz, Rsm = rosemaryite, Sam = samuelsonite, Scz = scorzalite, Trl = trolleite, Wrd = wardite. **B)** Raman spectra of phosphate minerals observed in the complex assemblage.

Raman images computed by univariate analysis, *i.e.* based on shifts in the position of single peaks, can show the distribution of individual phases. However, to reliably visualize the textures and spatial relations, multivariate analysis methods, which consider spectral variations in the complete spectral range, are necessary. Here, three types of multivariate analysis are compared: 1) supervised classical least squares (CLS) fitting, 2) unsupervised principal components analysis (PCA), and 3) unsupervised multivariate curve resolution (MCR). The CLS algorithm can discriminate all seven phases found with Raman point analysis (Figure 5A). The reference values used as inputs were derived from the map dataset itself, selecting the spectrum with the most indicative peaks and the highest signal-to-noise ratio, as the reference spectrum. In general, the CLS image is very similar to the optical photomicrograph (Figure 4A), having a good correlation of spectral data and position. It clearly discriminates the samuelsonite surrounding rosemaryite and filling some of its fractures. It can also distinguish the members of the scorzalite-lazulite series, showing the Mg-rich domains closer to rosemaryite and the Fe-rich domains closer to trolleite. Area percentage

distribution show that rosemaryite (0.133 mm^2, 32.5%) and trolleite (0.118 mm^2, 28.9%) make up most of the mapped surface, followed by lazulite (0.037 mm^2, 9.1%), samuelsonite (0.036 mm^2, 8.8%), quartz (0.034 mm^2, 8.3%), scorzalite (0.028 mm^2, 6.8%), and wardite (0.023 mm^2, 5.6%).

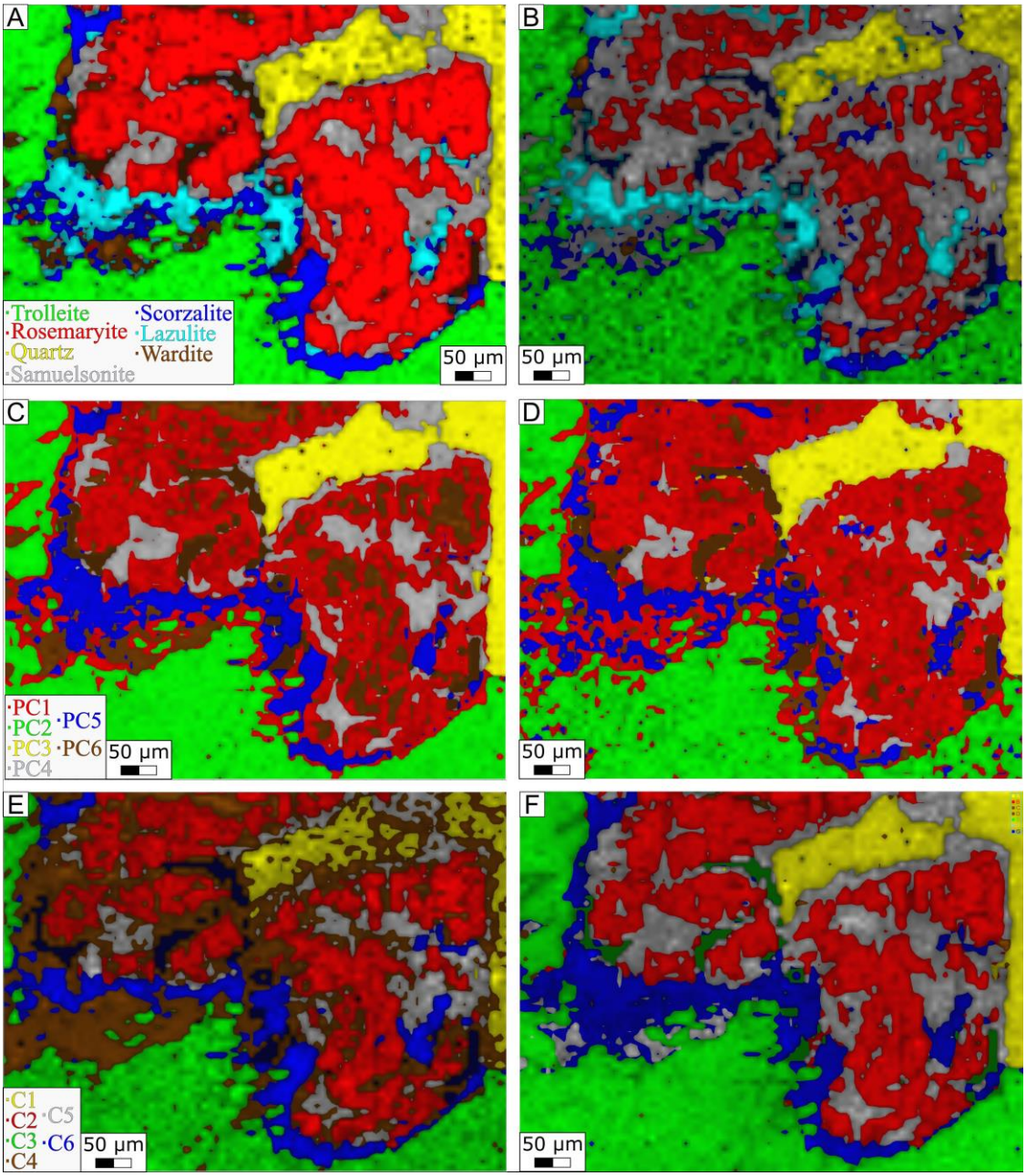

Figure 5: Case study 2 Raman mapping of the complex phosphatic assemblage from the Buranga pegmatite. **A)** and **B)** CLS output maps from the fully treated dataset (A) or the baseline-corrected dataset (B). **C)** and **D)** PCA output maps from the fully treated dataset (C) or the baseline-corrected dataset (D). **E)** and **F)** MCR output maps from the fully treated dataset (E) or the baseline-corrected dataset (F).

The effect of spectra processing on the output image of the multivariate analysis is assessed by comparing the results of a fully treated dataset (Figure 5A) with a dataset where only baseline correction was performed (Figure 5B). The fully treated dataset returns a much clearer image output under the CLS algorithm and shows a high correlation with the optical photomicrograph. The same is not valid for the low treatment dataset, whose image is rather spatially disordered and does not correlate with the optical photomicrograph.

The unsupervised analyses (*i.e.* PCA and MCR) do not provide good results for the complex phosphate assemblage. Firstly, they can recognize only up to six components, failing to differentiate between the scorzalite and lazulite members and reporting both phases as one component. Even if the number of components is increased, the algorithms will detect noise data before separating the two members. Secondly, the output images do not show a good correlation with the optical photomicrograph, rather showing chaotic phase distribution. Lastly, the unsupervised algorithms can result in nonrealistic phases where they are not present in reality, a serious problem that may create false impressions. The effect of processing on the unsupervised methods is the opposite of the one observed for the CLS. For both PCA and MCR, the low treatment dataset (Figure 5D and F, respectively) returns slightly more accurate images than the fully treated dataset (Figure 5C and E, respectively). However, the final outputs are still not as accurate as of the CLS image after the full treatment.

5. DISCUSSION

The sequence in which a mineral crystallizes in relation to other phases is called paragenesis. The paragenesis is a reflection of the interaction of the starting composition with the physicochemical conditions of the environment (*i.e.* temperature, pressure, pH, oxygen fugacity, presence of an aqueous fluid phase, and the composition of this fluid). This sequence should be the same for similar systems, regardless of the time or place it occurs, considering that the initial composition and environmental conditions are alike[4]. Therefore, establishing a mineral paragenesis is one way to assess the conditions of mineral formation, and directly reconstruct the evolutionary history of rocks. In the Buranga pegmatite, we are studying a crystallizing magmatic to magmatic-hydrothermal system. The crystallization of a highly fractionated magma, which is already enriched in incompatible elements, results in a complex paragenetic sequence and a high number of phosphate minerals described in pegmatites[4,23,24,26,37,78]. The first minerals to crystallize (primary) react with the residual fluids as crystallization progresses, and are replaced by metasomatic phases. Subsequently, when external water infiltrates through fractures in the rock, it further transforms the previous minerals into low-temperature phases. This paragenesis exemplifies a sequence of chemical reactions that occur during cooling, such as leaching of elements (*e.g.* Li, F), hydration, oxidation, and other cation exchanges (*e.g.* Na, Ca, Fe, Mn, Ba)[3,4,15,24,56,79].

The previous sections have shown the application of Raman imaging to investigate complex mineral assemblages and analyze their spatial distribution. The technique is capable of identifying even complex and accessory phosphate phases and their textural relations. In this section, the information obtained with the Raman maps is used to constrain the mineral evolution in phosphatic assemblages. The composition and spatial distribution of these minerals can be combined to define their sequence of formation (*i.e.* paragenesis).

In the first case study, the studied sample consists essentially of montebrasite [$LiAl(PO_4)(OH,F)$] with varying contents of F. Textural relations show that F-rich montebrasite, which occurs as irregular and corroded cores, is the primary mineral in the sequence, while the F-poor montebrasite represents a later, secondary mineral. One hypothesis for their genesis is that the primary F-rich montebrasite is magmatic in origin, and after its crystallization, it is progressively hydrated by the interaction with hydrothermal fluids. This hydration transforms it into the F-poor montebrasite, which dominates the internal parts of fractures representing high permeability zones. In this scenario, the F-moderate montebrasite delimits a partially altered zone which has experienced some secondary hydration, but not enough to extensively leach the initial F content. Another hypothesis is that the F-poor montebrasite is purely hydrothermal (*i.e.* newly grown phase precipitated directly from the fluid), without relation to the primary F-rich montebrasite. Based on our results, the first model is favored since all phases observed show optical continuity, have the same cleavage directions and crystal orientation (Figure 3A), and the transition between the two extreme compositions is always continuous and not truncated as it would be expected from a newly grown mineral.

Amblygonite and F-rich montebrasite (~4 – 6.5 mass% F or 3.9 – 6.3 mol% F) are commonly the primary, higher temperature phases in pegmatites[76,78]. Primary amblygonite-montebrasite is known to be prone to replacement by a large range of products, from simple hydration to form F-poor montebrasite, to Li-leaching and addition of external elements (*e.g.* Na, Ca, Fe) to make up complex phosphate minerals[4,25,63,78]. However, in this study, no other phases were observed at the studied scale. Consequently, the replacement of primary F-rich montebrasite by secondary F-poor montebrasite represents a progressive hydration process with concomitant F-leaching by the fluid phase, represented by the F-OH exchange reaction: $LiAl(PO_4)(OH,F) \rightarrow LiAl(PO_4)OH$, or simply $F^- \rightarrow OH^-$. The other elements (Li, Al, and PO_4) remain in the same amounts.

The observed F content (1.7 to 6.6 mol%) is similar to the range defined by previous studies in the Buranga pegmatite[80,81]. However, the low-F side (<3 mol%), corresponding to the F-poor montebrasite in microfractures, has never been documented to our knowledge. This might be a reflection of the bulk analyses conducted in the past, which generated an average value of the host phase (F-rich) and the fracture material (F-poor). This issue highlights the necessity to apply high spatial resolution techniques to identify the phases. Only by high resolution *in situ* measurements can the signal of both host phases and the fracture mineral be separated and interpreted, as is shown in the present study.

The second case study represents a complex phosphate assemblage, where trolleite [$Al_4(PO_4)_3(OH)_3$] and rosemaryite [$\square Na(Mn,Fe)Fe^{3+}Al(PO_4)_3$] show corroded borders and are penetrated by paragenetic younger minerals, thus representing the earlier phases. One problem that arises is that rosemaryite is too oxidized to be a primary phase[39]. Some authors proposed that wyllieite [$Na_2(Mn,Fe)Fe^{2+}Al(PO_4)_3$] is a common primary mineral and that rosemaryite forms by its oxidation[39,64]. In the studied case, Wyllieite

does occur as inclusions in quartz and trolleite in the same sample, but there are no indications of a direct relation between wyllieite and rosemaryite, neither as relics of wyllieite inside rosemaryite nor as signs of replacement of the former by the latter to confirm this oxidation reaction.

The initial minerals were subsequently replaced by lazulite [$(Mg,Fe)Al_2(PO_4)_2(OH)_2$] and scorzalite [$(Fe,Mg)Al_2(PO_4)_2(OH)_2$], that is, trolleite and rosemaryite reacted with each other, and possibly with a fluid phase, to form lazulite and scorzalite. As the stability field of lazulite is experimentally determined to be at higher temperatures than that of scorzalite[20], lazulite is interpreted as the first phase to form, preferentially consuming Mg from rosemaryite and increasing the Fe/Mg ratio of the system. Subsequently, when the Fe/Mg ratio was high enough, scorzalite became the stable phase. Samuelsonite [$Ca_9(Fe,Mn)_4Al_2(PO_4)_{10}(OH)_2$] occurs only associated with rosemaryite, surrounding it and filling its fractures (Figure 5). The absence of Ca in other minerals of the assemblage imposes that this element was externally introduced into the system, probably remobilized within the rock by a fluid phase from areas that host Ca-minerals, such as apatite [$Ca_5(PO_4)_3(OH,F)$]. The replacement of rosemaryite by lazulite-scorzalite releases Na to the system, since the Na present in rosemaryite's structure does not fit inside the lazulite-scorzalite. This excess Na could then react with the adjacent trolleite and possibly a fluid phase, which would provide the surplus water content, to form wardite [$NaAl_3(PO_4)_2(OH)_4 \cdot 2H_2O$].

Accordingly, the mineral sequence of this assemblage from the phosphatic nodule from Buranga is trolleite + rosemaryite → lazulite-scorzalite → samuelsonite → wardite (Figure 1). This sequence indicates that the mineral reaction trolleite + rosemaryite → lazulite-scorzalite is followed by an input of Ca to the system, generating samuelsonite around rosemaryite. Afterward, when the temperature is lower and the water activity is higher, wardite becomes stable.

In both cases studied, the distinction between the phases is considerably better with the CLS algorithm. Unsupervised methods that automatically select the components (in this case, PCA and MCR methods) are unable to distinguish all minerals present and to correctly show their spatial distribution. These problems might indicate an inability of the unsupervised methods to analyze non-ideal datasets such as natural minerals and geological reactions, especially for maps of complex assemblages with low acquisition time on each spot (less than one second). Consequently, supervised methods are favored in the study of mineral paragenesis, and unsupervised methods should be used only as intermediate steps to assess the mapping dataset. Figure 6 shows the suggested workflow for paragenetic studies of complex mineralogical assemblages using Raman mapping.

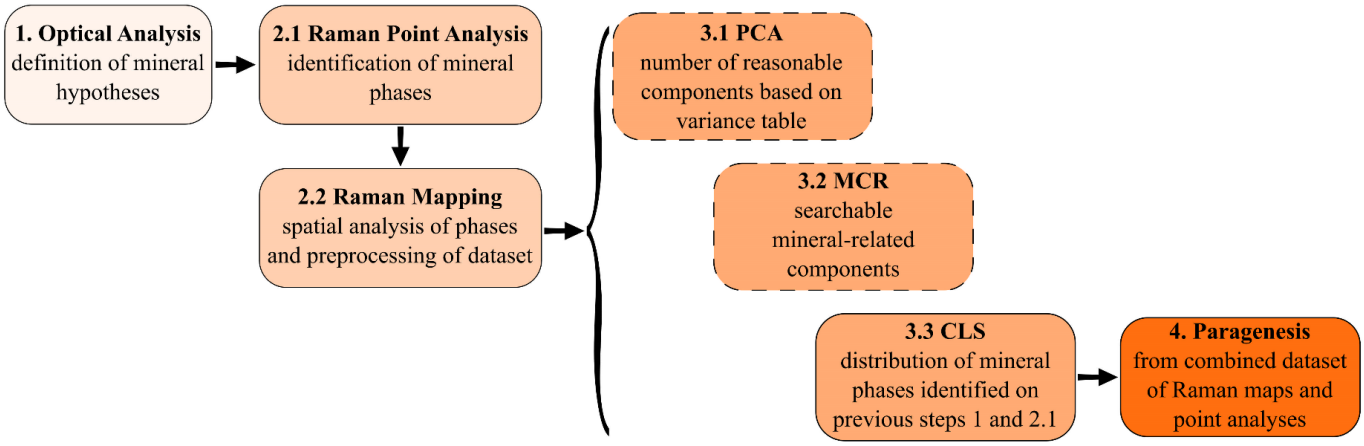

Figure 6: Flowchart of suggested steps to develop mineral paragenetic sequences using Raman images.

6. IMPLICATIONS

Raman mapping of complex mineral assemblages can successfully characterize their paragenesis, opening many opportunities to apply this technique in different assemblages within rock samples. This visual and spectroscopic aid can significantly improve the interpretation of complex assemblages and helps in the development of pressure-temperature-composition (P-T-X) models.

Both amblygonite and montebrasite are sources of Li, representing important ores for the growing battery industry. Consequently, it is important for resource estimation and ore processing to evaluate alteration products in a given sample and to assess the spatial presence of impurities.

The analyzed Buranga sample can still be considered a Li ore, as it is entirely composed of either primary F-rich montebrasite, secondary F-poor montebrasite, or a transition between both, without the major presence of contaminant elements, such as Fe, Mg, Ca, Na, and K[11], in the examined scale. Furthermore, the presence of F can complicate the processing of these phosphate Li-ores[12], as the release of F gases, such as HF, during the processing route can have serious environmental impacts, imposing higher costs for filtering of ores with high F content. Raman mapping of these minerals can help in the search of high-quality Li-ore samples since it easily shows preferential regions with lower F content that are suitable for extraction.

Raman imaging can identify all the phases involved and can be used to assess their textural relations, showing that there is progressive hydration of the primary F-rich montebrasite, replacing it by a F-poor montebrasite. Furthermore, Raman imaging can be used to distinguish the involved phases with higher precision than regular optical microscopy or even electron microscopy, and without sample preparation that other methods require.

For the complex phosphatic assemblage of case study 2, mineral paragenesis shows that higher temperature phases are transformed into intermediate temperature phases and then to low-temperature phases. These mineral reactions are assisted by the presence of a fluid phase that remobilizes the chemical

elements and at the same time hydrates and oxidizes the minerals. Combining both assemblages studied, a general trend of progressive hydration, followed by internal remobilization of elements, such as F, Na, Li, and addition of Ca into the system, is suggested to have occurred during cooling of the Buranga pegmatite.

Follow up studies with FTIR mapping can supplement the analysis of OH-bearing phosphates and help the refinement of the paragenesis

7. CONCLUSION

This study shows that Raman mapping is a powerful micro-analytical technique to investigate complex mineral assemblages and their paragenetic sequence. It can unequivocally identify major and accessory phases and image their spatial relations *in situ* with high resolution. Raman maps of phosphate mineral assemblages successfully show their sequence of formation, which in turn reflects the fractionation process of pegmatitic magmas during cooling.

Multivariate analyses are preferred over univariate, as accurate spectral distinctions can only be made by considering the whole spectrum and not only single peaks, especially for complex assemblages. Unsupervised classification methods do not correctly represent all phases present in the mapped area, neither their real spatial distribution. Therefore, a user-mediated classification is recommended. Both continuous (*e.g.* peak positions and FWHM) and discrete (*e.g.* mineral zones) classification images can be generated, depending on the desired information from the dataset.

In the case of complex mineral assemblages, we advise that an optical analysis should be carried before Raman mapping. This helps in the identification of mineral phases and zones within the sample, which will guide the Raman map analysis. Subsequently, these mineral phases should be applied as reference values in supervised multivariate analysis algorithms to create Raman images. Finally, the paragenetic sequence can be drawn from the interpretation of the Raman images.

ACKNOWLEDGEMENTS

The financial support for this research comes from KU Leuven, in the form of a PhD scholarship for Fernando Prado Araujo. Research of Niels Hulsbosch is supported by a Junior Postdoctoral Fellowship of the FWO. The Raman equipment of KU Leuven was acquired via the medium-scale research infrastructure grant Raman-SIM2 (grant no I000718N). The authors appreciate the careful reviews and comments by the editor and three anonymous reviewers that improved the manuscript. We are grateful to Prof. Dr. Stijn Dewaele (UGent), Dr. Florias Mees (Royal Museum for Central Africa), and Prof. Dr. Frédéric. Hatert (ULiège) for providing the Buranga phosphate samples. Herman Nijs (KU Leuven) is thanked for preparing the high-quality thin sections, wafers, and polished slabs. Prof. Dr. Jan Elsen (KU Leuven) is acknowledged

for access to the Bosman mineral collection at KU Leuven. The assistance of Tobias Hendricks (KU Leuven) with the Bosman mineral collection analyses is much appreciated. Philippe Muchez, Niels Hulsbosch, and Fernando Prado Araujo are members of KU Leuven Institute for Sustainable Metals and Minerals.

REFERENCES

[1] Mindat, https://www.mindat.org/element/Phosphorus.

[2] P. Quensel, *Geol. Fören. Stockholm Förh* **1937**, *59*, 77.

[3] D. J. Fisher, *Am. Mineral.* **1958**, *43*, 181.

[4] P. B. Moore, *Mineral. Rec.* **1973**, *4*, 103.

[5] J. O. Nriagu, P. B. Moore, *Phosphate Minerals*, Springer, Berlin Heidelberg, **1984**.

[6] P. B. Moore, *Mineral. Assoc. Can. Short Course Ser.* **1982**, *8*, 267.

[7] D. Sustainability, British Geological Survey, Bureau de Recherches Géologiques et Minières, N. O. for A. S. Research, *Study on the review of the list of Critical Raw Materials Criticality Assessments*, Brussels, **2017**.

[8] G. H. McClellan, L. R. Gremillion, in *The Role of Phosphorus in Agriculture*, (Eds: F. E. Khasawneh, E. C. Sample, E. J. Kamprath), American Society of Agronomy, Madison, Wisconsin, USA, **1980**, pp. 43–80.

[9] Y. Taha, M. Benzaazoua, *Minerals* **2019**, *9*, 10.

[10] R. L. Linnen, M. Van Lichtervelde, P. Černý, *Elements* **2012**, *8*, 275.

[11] A. Chagnes, J. Swiatowska, *Lithium Process Chemistry*, Elsevier, Amsterdam, Netherlands, **2015**.

[12] P. F. A. Braga, S. C. A. França, C. C. Gonçalves, P. F. V Ferraz, *Hydrometallurgy* **2020**, *191*, 105249.

[13] D. London, G. B. Morgan VI, M. B. Wolf, *Am. Mineral.* **2001**, *86*, 225.

[14] D. London, M. B. Wolf, G. B. Morgan VI, M. G. Garrido, *J. Petrol.* **1999**, *40*, 215.

[15] C. Rao, R. Wang, Y. Yang, F. Hatert, Q. Xia, X. Yue, W. Wang, *Ore Geol. Rev.* **2017**, *91*, 864.

[16] D. E. Harlov, *Elements* **2015**, *11*, 171.

[17] T. Llorens, M. C. Moro, *Mineral. Mag.* **2012**, *76*, 1.

[18] F. Hatert, in *Minerals as Advanced Materials II*, (Ed: S. V. Krivovichev), Springer-Verlag, Berlin Heidelberg, **2012**, pp. 279–291.

[19] F. Hatert, L. Ottolini, P. Schmid-Beurmann, *Contrib. Mineral. Petrol.* **2011**, *161*, 531.

[20] P. Schmid-Beurmann, S. Knitter, L. Cemič, *Mineral. Petrol.* **2000**, *70*, 55.

[21] J. D. Bass, C. B. Sclar, *Am. Mineral.* **1979**, *64*, 1175.

[22] K. Drüppel, A. Hösch, G. Franz, *Am. Mineral.* **2007**, *92*, 1695.

[23] M. Á. Galliski, P. Černý, M. F. Márquez-Zavalía, R. Chapman, *Can. Mineral.* **2012**, *50*, 933.

[24] M. Baijot, F. Hatert, S. Philippo, *Can. Mineral.* **2012**, *50*, 1531.

[25] J. R. Baldwin, P. G. Hill, O. von Knorring, G. J. H. Oliver, *Mineral. Mag.* **2000**, *64*, 1147.

[26] E. Roda, A. Pesquera, F. Fontan, P. Keller, *Am. Mineral.* **2004**, *89*, 110.

[27] F. Hatert, *Eur. J. Mineral.* **2019**, *2*, 807.

[28] J. M. Pyle, F. S. Spear, D. A. Wark, *Rev. Mineral. Geochem.* **2002**, *48*, 337.

[29] J. C. Stormer, M. L. Pierson, R. C. Tacker, *Am. Mineral.* **1993**, *78*, 641.

[30] A. Watenphul, M. Burgdorf, J. Schlüter, I. Horn, T. Malcherek, B. Mihailova, *Am. Mineral.* **2016**, *101*, 970.

[31] P. F. McMillan, G. H. Wolf, B. T. Poe, *Chem. Geol.* **1992**, *96*, 351.

[32] B. Rondeau, E. Fritsch, P. Lefèvre, M. Guiraud, A.-M. Fransolet, Y. Lulzac, *Can. Mineral.* **2006**, *44*, 1109.

[33] K. D. Litasov, N. M. Podgornykh, *J. Raman Spectrosc.* **2017**, *48*, 1518.

[34] R. L. Frost, W. Martens, P. A. Williams, J. T. Kloprogge, *Mineral. Mag.* **2002**, *66*, 1063.

[35] L. Nasdala, D. C. Smith, R. Kaindl, M. A. Ziemann, in *EMU Notes in Mineralogy*, (Eds: A. Beran, E. Libowitzky), Eotvos University Press, Budapest, **2004**, vol. 6, pp. 281–343.

[36] V. D. C. Daltry, O. von Knorring, *Geol. Belg.* **1998**, *1*, 9.

[37] A.-M. Fransolet, *Mineral. Mag.* **1980**, *43*, 1015.

[38] A.-M. Fransolet, O. von Knorring, F. Fontan, *Bull. Geol. Soc. Finl.* **1992**, *64*, 13.

[39] A.-M. Fransolet, *Eur. J. Mineral.* **1995**, *7*, 567.

[40] F. Hatert, P. Keller, F. Lissner, D. Antenucci, A.-M. Fransolet, *Eur. J. Mineral.* **2000**, *12*, 847.

[41] F. Hatert, A.-M. Fransolet, W. V. Maresch, *Contrib. Mineral. Petrol.* **2006**, *152*, 399.

[42] A.-M. Fransolet, P. Tarte, *Am. Mineral.* **1977**, *62*, 559.

[43] O. von Knorring, T. G. Sahama, *Schweiz. Mineral. Petrogr. Mitt.* **1982**, *62*, 343.

[44] P. Schmid-Beurmann, L. Ottolini, F. Hatert, T. Geisler, M. Huyskens, V. Kahlenberg, *Mineral. Petrol.* **2013**, *107*, 501.

[45] S. Dewaele, F. Henjes-Kunst, F. Melcher, M. Sitnikova, R. Burgess, A. Gerdes, M. Fernandez-Alonso, F. de Clercq, P. Muchez, B. Lehmann, *J. Afr. Earth Sci.* **2011**, *61*, 10.

[46] P. Muchez, N. Hulsbosch, S. Dewaele, *Bull. Séanc. Acad. R. Sci. Outre-Mer* **2014**, *3–4*, 515.

[47] N. Hulsbosch, J. Hertogen, S. Dewaele, L. André, P. Muchez, *Geochim. Cosmochim. Acta* **2014**, *132*, 349.

[48] D. London, *Lithos* **2014**, *184–187*, 74.

[49] N. Hulsbosch, P. Muchez, *Lithos* **2020**, *354–355*, 105285.

[50] J. Van Daele, N. Hulsbosch, S. Dewaele, P. Muchez, *J. Afr. Earth Sci.* **2020**, *165*, 103783.

[51] J. Dubessy, M.-C. Caumon, F. Rull, S. Sharma, in *Raman Spectroscopy applied to Earth Sciences and Cultural Heritage*, (Eds: J. Dubessy, M.-C. Caumon, F. Rull), The European Mineralogical Union; The Mineralogical Society of Great Britain & Ireland, EMU Notes., **2012**, vol. 12, pp. 83–172.

[52] G. Gouadec, L. Bellot-Gurlet, D. Baron, P. Colomban, in *Raman imaging*, (Ed: A. Zoubir), Springer, Berlin, Heidelberg, **2012**, pp. 85–118.

[53] L. Nasdala, O. Beyssac, J. W. Schopf, B. Bleisteiner, in *Raman imaging*, (Ed: A. Zoubir), Springer, Berlin Heidelberg, **2012**, pp. 145–187.

[54] J. H. Parker, D. W. Feldman, M. Ashkin, *Phys. Rev.* **1967**, *155*, 712.

[55] M. Vidal, J. M. Amigo, *Chemom. Intell. Lab. Syst.* **2012**, *117*, 138.

[56] F. C. Hawthorne, *Mineral. Mag.* **1998**, *62*, 141.

[57] P. B. Moore, *Am. Mineral.* **1965**, *50*, 2052.

[58] D. M. C. Huminicki, F. C. Hawthorne, *Rev. Mineral. Geochem.* **2002**, *48*, 123.

[59] I. D. Brown, in *Structure and Bonding in Crystals II*, (Eds: M. O'Keeffe, A. Navrotsky), Academic Press, New York, **1981**, pp. 1–30.

[60] S. J. Omelon, M. D. Grynpas, *Chem. Rev.* **2008**, *108*, 4694.

[61] D. E. C. Corbridge, *Bull. Soc. Fr. Mineral. Cristallogr.* **1971**, *94*, 271.

[62] S. D. Ross, in *Mineralogical society monograph 4: the infrared spectra of minerals*, (Ed: V. C. Farmer), The Mineralogical Society, London, **1974**, pp. 383–422.

[63] Y. Shirose, S. Uehara, *J. Mineral. Petrol. Sci.* **2014**, *109*, 103.

[64] F. Hatert, M. Á. Galliski, E. Roda-Robles, P. Vignola, A.-M. Fransolet, *Can. Mineral.* **2016**, *54*, 1087.

[65] W. P. Griffith, *Nature* **1969**, *224*, 264.

[66] M. Barj, H. Perthuis, P. Colomban, *Solid State Ionics* **1983**, *11*, 157.

[67] M. Barj, H. Perthuis, P. Colomban, *Solid State Ionics* **1983**, *9–10*, 845.

[68] W. Jastrzebski, M. Sitarz, M. Rokita, K. Bułat, *Spectrochim. Acta, Part A* **2011**, *79*, 722.

[69] R. M. Almeida, S. Höfer, T. G. Mayerhöfer, J. Popp, K. Krambrock, R. P. S. M. Lobo, A. Dias, R. L. Moreira, *Vib.*

Spectrosc. **2015**, *77*, 25.

[70] L. A. Groat, M. Raudsepp, F. C. Hawthorne, T. S. Ercit, B. L. Sherriff, J. S. Hartman, *Am. Mineral.* **1990**, *75*, 992.

[71] J. W. Anthony, R. A. Bideaux, K. W. Bladh, M. C. Nichols, Handbook of Mineralogy, http://www.handbookofmineralogy.org/.

[72] A. N. Winchell, *Am. Mineral.* **1926**, *11*, 246.

[73] I. Černá, P. Černý, R. B. Ferguson, *Am. Mineral.* **1973**, *58*, 291.

[74] E. H. Nickel, *Am. Mineral.* **1992**, *77*, 660.

[75] L. A. Groat, B. C. Chakoumakos, D. H. Brouwer, C. M. Hoffman, C. A. Fyfe, H. Morell, A. J. Schultz, *Am. Mineral.* **2003**, *88*, 195.

[76] I. Černá, P. Černý, R. B. Ferguson, *Can. Mineral.* **1972**, *11*, 643.

[77] F. Hatert, G. J. Long, D. Hautot, A.-M. Fransolet, J. Delwiche, M. J. Hubin-Franskin, F. Grandjean, *Phys. Chem. Miner.* **2004**, *31*, 487.

[78] D. London, D. M. Burt, *Am. Mineral.* **1982**, *67*, 97.

[79] E. Roda-Robles, R. Vieira, A. Pesquera, A. Lima, *Mineral. Petrol.* **2010**, *100*, 23.

[80] J. Dubois, J. Marchand, P. Bourguignon, *Ann. Soc. Geol. Belg.* **1973**, *95*, 285.

[81] A.-M. Fransolet, K. Abraham, *Ann. Soc. Geol. Belg.* **1983**, *106*, 299.